Diffusion of muonic deuterium and hydrogen atoms

D. J. Abbott,* G. F. Chen,† P. Guss,‡ A. D. Hancock, J. B. Kraiman,§ R. T. Siegel, W. F. Vulcan,* D. W. Viel, and R. E. Welsh
College of William and Mary in Virginia, Williamsburg, Virginia 23185

C. Petitjean and A. Zehnder
Paul Scherrer Institute, CH-5232 Villigen PSI, Switzerland

W. H. Breunlich, M. Cargnelli, P. Kammel,‖ A. Scrinzi, J. Marton, and J. Zmeskal
Institut für Mittelenergiephysik, Österreichische Akademie der Wissenschaften, A-1090 Vienna, Austria

J. J. Reidy and H. L. Woolverton¶
University of Mississippi, University, Mississippi 38667

F. J. Hartmann
Technische Universität München, D-85748 Garching, Germany

A. Adamczak
Institute for Nuclear Physics, PL-31-342 Cracow, Poland

V. E. Markushin **
Russian Scientific Center, Kurchatov Institute, RU-123182 Moscow, Russia

V. S. Melezhik
Joint Institute for Nuclear Research, RU-141980 Dubna, Russia

(Received 15 January 1996; revised manuscript received 20 September 1996)

Diffusion of muonic deuterium μd and muonic hydrogen μp atoms produced following the stopping of negative muons in D_2 or H_2 at 300 K was studied at pressures of 47–750 mbar (H_2) and 94–1520 mbar (D_2) in two distinct target geometries. Time intervals were recorded between entry of negative muons into the gas and arrival of each resulting μd or μp atom at one of 50 foils immersed in the gas, and spaced regularly along the muon beam axis. The results of such measurements were fitted to time distributions generated by Monte Carlo methods, using theoretical scattering predictions and empirically chosen forms for the initial energy distributions of the muonic atoms in the $1S$ state. Results indicate muonic atom energy distributions which (a) are different for μd and μp and (b) vary with pressure. The best-fit energy distributions have mean energies ranging from 1.5 eV for μd at 94 mbar to $\geqslant$9 eV for μp at 750 mbar. The data are also sensitive to scattering cross sections for μd and μp, and are consistent with current theoretical calculations for the $\mu d + D_2$ cross sections. In the case of $\mu p + H_2$ scattering, the experimental data suggest discrepancies with the theoretical predictions. [S1050-2947(97)06501-3]

PACS number(s): 36.10.Dr

I. INTRODUCTION

Muonic hydrogen atoms (μp, μd, or μt) are formed when negative muons are brought to rest in targets filled with pure or mixed hydrogen isotopes in gaseous, liquid, or solid form. (It is also possible that muons stopping in hydrogen compounds, e.g., CH_4, will form free μp atoms, but no experimental evidence for this exists at present.) Such muonic atoms, being analogous to ordinary hydrogen atoms, provide opportunity for study of QED, weak interactions, and atomic scattering processes. However, the distance scale for muonic hydrogen is smaller by a factor m_e/m_μ than the usual Bohr atomic scale, which affects calculations of muonic hydrogen properties and also leads to the remarkable phenomenon of muon catalyzed fusion (μCF) discovered by Alvarez *et al.* [1].

*Present address: TJNAF(formerly CEBAF), Newport News, VA 23606.
†Present address: Chongqing Institute of Architecture and Engineering, Chongqing, Sichuan, People's Republic of China.
‡Present address: EGG Energy Measurements, Suitland, MD 20746.
§Present address: Dynamics Technology Inc., Arlington, VA 22209.
‖Present address: University of California and LBNL, Berkeley, CA 94720.
¶Present address: University of Central Arkansas, Conway, AZ 72035.
**Present address: Paul Scherrer Institute, CH-5232 Villigen PSI, Switzerland.

In studying muonic hydrogen atom processes, it is necessary to establish the initial states from which the processes occur. For example, if it is desired to measure the weak pseudoscalar form factor in muon absorption of protons ($\mu^- + p \rightarrow n + \nu_\mu$) in the triplet state of the μp atom, then it is necessary to understand the evolution of hyperfine state populations of μp atoms after the atoms are formed in the target. This in turn requires understanding the initial energy distribution of these atoms, and their cross sections for scattering off the molecules of the target. Monoenergetic beams of μp atoms in vacuum are not currently available for such studies. (We note, however, that μd and μt atoms of about 1 eV kinetic energy can now be produced in vacuum using frozen hydrogen targets [2]). Thus the only practical approach to measuring the initial energy distribution and the scattering is to deduce them from experiments on the interactions of the μp atoms in the target gas itself, i.e., by studying the way in which single μp atoms progress through the target gas. The neutrality and small size ($\sim 2.5 \times 10^{-11}$ cm) of the muonic atoms suggest that the techniques for studying the diffusion of neutrons of similar energy (≈ 1 eV) are appropriate. For example, the main experimental work to date on scattering and energy spectrum determination for muonic hydrogen atoms has involved measurement of the time distributions of muonic atoms diffusing through a target until they strike a boundary, at which time the muon transfers to an atom of the wall material and a characteristic radiation is emitted from the new muonic atom.

The first muonic hydrogen diffusion experiment was performed at CERN and reported in 1967 [3]. Negative muons from a secondary beam of pions at the CERN synchrocyclotron were stopped in a chamber filled with hydrogen gas and containing an array of parallel thin foils or plates of Au. When the muons stopped in the gas, μp atoms were formed; many of these diffused to the Au foils, though some decayed en route. The time distribution of μp's striking the foils was obtained by measuring the time intervals between muons entering the chamber and muonic Au K-series x rays emitted when the μp or μd atoms struck foils and the muons were transferred from the protons to the Au nuclei. This time distribution was then compared to calculated time distributions obtained by making specific assumptions about the initial energy distributions of the μp and the scattering cross sections. Because of the limitations on proton beam current (≈ 1 μA) at the time of the CERN experiments, the number of muons/s which could be stopped in a dilute gas was quite limited, so that the experiment had to be done mostly at a pressure of 26 bars of H_2, with a small portion of the data being taken at 10 bars. In the late 1970s a second set of diffusion experiments was undertaken at CERN by Bertin *et al.* [4], though in this case the foil array was of Al rather than Au. The motivation for all the CERN experiments was to establish the experimental conditions (target dimensions, pressure, temperature) suitable for studying ordinary muon capture in μp atoms. That was also the motivation for the experiments reported here.

The advent of meson factories and their proton beam currents of 0.1–1.0 mA have made possible refinements of the CERN experiments on muonic hydrogen atom diffusion. Sensitivity and signal-to-noise ratio were enhanced in this experiment by (a) use of intrinsic Ge photon detectors with their superior resolution compared to NaI(Tl), and (b) use of foils composed of thin (9 μm) plastic sheet with 100-Å-thick Au layers on both sides. Such foils give a low background from muons stopping directly in the Au, while muonic hydrogen atoms impacting the foils were readily stopped by the Au (cf. Sec. II below). In the present experiment, which was done at the Paul Scherrer Institute (PSI), it was possible to obtain statistically significant data at pressures down to 47 mbar of H_2, while still having good signal-to-noise ratio. This permitted taking data over a range of pressures and with two different spacings between the foils. Our goal was to work from pressures low enough so that a μp (or μd) atom would suffer little scattering before striking a foil, to pressures high enough so that the effects of scattering of the μp or μd as they moved between the foils could be clearly seen in the data. At the lower pressures one should presumably be able to see evidence for the initial energy distribution. At the higher pressures, the behavior of the scattering cross sections vs energy could be compared to theoretical predictions. In general these expectations were borne out, though the evidence which developed for a pressure, i.e., density dependence of the initial energy distribution complicated interpretation to some degree.

The use of two different foil spacings provided a test of internal consistency in the experiment, because in principle the rates for physical processes at a fixed pressure cannot depend on the geometry of the target. Thus calculated results for such physical quantities as μp initial kinetic energies at fixed pressure should be consistent at different foil spacings. However, the spatial distributions of stopping muons may exhibit characteristics which could appear to invalidate this conclusion. For example, we assumed during our analysis that muons stopped uniformly in the target gas volumes, but in fact there could be voids in the stopping distributions just downstream of each foil. It is difficult to eliminate, or even to test, such conjectures, for to do so would involve the introduction of new parameters beyond those central to the analysis and thus increase the uncertainties for those parameters of greatest physical interest. In the case of the hypothetical voids mentioned above, we were able to search our results for evidence of their occurrence, and found none. In the final analysis of the data the stopping was therefore assumed uniform in the space between foils.

In a preliminary report [5] we described the μd part of the experiment and its interpretation based on theoretical cross sections available in the literature at the end of 1989. These cross sections were for scattering off *nuclei* only, whereas the targets were actually composed of molecular gases. In the intervening years the scattering theory has developed dramatically through inclusion of the effects of molecular binding, electron screening, etc., thus facilitating interpretation of the data and helping to improve understanding of the diffusion process [6].

In Sec. II the experimental apparatus, both mechanical and electronic, is described, followed in Sec. III by a description of the method of analysis of the experimental data. In Sec. IV the theory of the Coulomb scattering of muonic hydrogen atoms is reviewed, and in Sec. V the conclusions are described.

II. EXPERIMENTAL APPARATUS

A. Mechanical

As noted above, the basic principle of this experiment is that, unless they first decay, diffusing μp or μd atoms will eventually impact a wall of the target volume in which they were originally formed, and upon doing so will immediately transfer their muon to an atom of the material of which the wall is formed. For these atoms, the ordinary and radiative nuclear capture processes, and also the formation of muonic molecules or complexes, have rates negligible compared to decay or wall impact at the pressures used here. The muonic atoms formed by transfer at impact with the walls will deexcite with the emission of a characteristic spectrum. In our experiment there were 49 independent target volumes, each 10 cm in diameter and either 0.2286 or 0.4572 cm thick. Each volume was formed by a pair of foil faces composed of 9-μm Kynar ($C_2H_2F_2$) foil, a low-vapor-pressure plastic. The foils were stretched across and rf welded to Kynar spacer rings 0.2286 cm thick which formed the side wall of each cylindrical volume. Fifty foils, each with its outer ring, were stacked within an Al target vessel to form a sequence of coaxial target volumes which were later filled with hydrogen or deuterium (see Fig. 1). In order to double the space between foils on occasion, empty spacer rings were alternated with those carrying foils. Each foil had been coated by vapor deposition with 100 ± 10 Å of Au on both surfaces. It was this Au layer to which a μp which had been formed in a particular target volume would transfer its muon to form a muonic Au atom. Based on an extrapolation of the μp transfer rate to Xe as then known [7] we estimated the transfer cross section as 10^{-16} cm^2. The Au thickness was chosen to stop μp atoms of up to about 5 eV, because at the time this experiment was planned (1987), the expected energy of the μp atoms in their $1S$ state after the initial cascade was only about 1 eV, and there is other good reason for minimizing the thickness of the Au layer, as described above.

Measurements showed a $\pm5\%$ uniformity in spacing between the Kynar foils. Some beam muons stopping directly in the Au layers on the foils would also form muonic Au atoms and thus give transferlike signals in prompt coincidence with the scintillation counter signal from an incoming muon. These prompt coincidences formed a background in the early portions of the time distributions, and ultimately limited the pressure at which statistically useful data could be taken.

The pressure was held to within $\pm1\%$ of the nominal values. Temperature was monitored continuously and varied less than $\pm5\%$ from 300 K during the experiment. We therefore estimate that uncertainties in density were less than $\pm5\%$.

The Au layer on the Kynar foils had a surface layer of carbon some 5–10 Å thick, as is quickly formed on all Au surfaces under ambient conditions. We observed at D_2 pressure of 7.8 bars a delayed background of the $n=3\rightarrow n=1$ and $4\rightarrow1$ muonic carbon x rays, a background absent from the data accumulated at 2.5 bars or lower. We attributed this background to μd atoms degraded in energy by scattering at the higher pressures of the target gas to the point that they could be captured by the carbon layer before they reached the Au. By limiting our observation to pressures of both deuterium and hydrogen below 2.5 bars we thus avoided recording of delayed muonic x-ray backgrounds from carbon. Muonic fluorine x rays were also significant, because their presence might provide evidence for the penetration through the Au layer of some fast μp atoms. Therefore a search for such x rays was made [8]. Some muonic fluorine x rays were detected at a low level relative to the signals from the Au, but the time structure of the muonic fluorine x rays relative to incoming muons, and their higher relative intensities at lower pressures, led to the conclusion that they probably originated from beam muons which escaped ''second muon'' protective circuitry (see below) at about the 10^{-4} level, and stopped in the Kynar foils. Thus it was concluded that the Au layers on the Kynar foils in fact sufficed to stop all diffusing muonic hydrogen atoms, presumably because the atoms impinge on the foils in a directionally random distribution and because at the higher pressures substantial scattering and energy degradation of the atoms occur in the gas before foil impact.

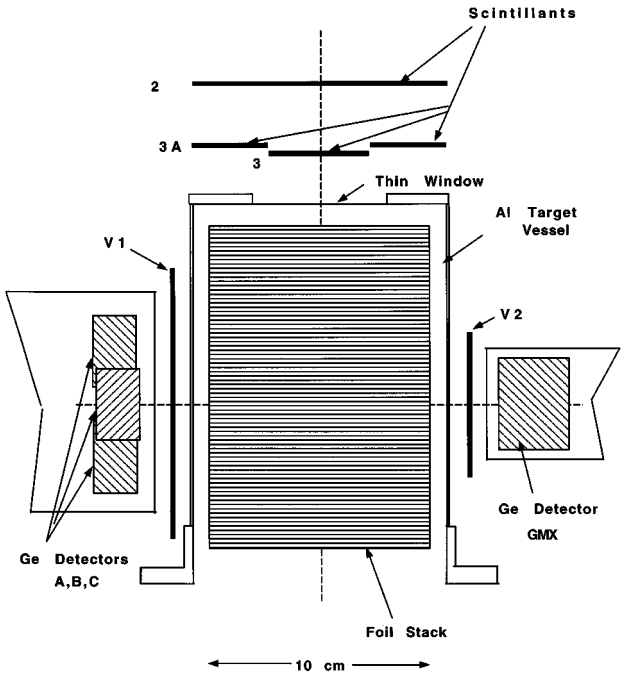

FIG. 1. Experimental setup. The negative muon beam (μE4 at PSI) entered from the top along the dashed center line. S_1–S_3 and V_1, V_2 are scintillation counters.

B. Detectors and electronics

The main detectors used are shown in Fig. 1. Their characteristics are summarized in Table I. Muon stops in the target were defined by three plastic scintillation detectors S_1, S_2, and S_3. S_1 detected the muons exiting the beam pipe, whereas S_2 and S_3 selected the desired beam geometry relative to the target. In particular, muons were only accepted when passing through the S_2 aperture, which had a diameter of 5 cm and was centered at the axis of the foil stack. This reduction of the beam diameter conservatively took into account the beam divergence and multiple scattering effects, so that a large majority of accepted muons would stop within the 10 cm diameter of the cylindrical foil stack. Thus the

TABLE I. Detector characteristics.

Detector	Type	Dimensions (cm)[a]
Plastic scintillation detectors		
S_1	NE-102A	20×20, $T=0.06$
S_2	NE-102A	18×14, $T=0.5$
S_3	NE-102A	$\Phi=5.5$, $T=0.05$
V_1	NE-102A	$\Phi=14$, $T=0.2$
V_2	NE-102A	8×8, $T=0.3$
High-purity Ge detectors		
A,B,C	intrinsic, planar	$\Phi=4.7$, $T=2.6$ each
GMX	intrinsic, modified coaxial	$\Phi=4.9$, $T=4.4$
Neutron detector	NE-213 liquid scintillant	$\Phi=12.7$, $T=10.16$

[a]Φ denotes the diameter, T the thickness of the detector.
[b]With $\Phi=5$ cm aperture.

''μ-stop'' signal was defined by the electronic coincidence $S_1\cdot S_2\cdot S_3$. After being placed in anticoincidence with the various system deadtimes, this signal initiated the data taking by opening a 5-μs-long ''event gate'' and by starting the TDC's (time-to-digital-converters).

As explained above, the basic signatures for muonic hydrogen diffusion to a foil surface were x rays and nuclear γ rays emitted after muon transfer to heavier nuclei. These were detected by four high-resolution intrinsic germanium detectors. Detectors A, B, and C were housed in a single vacuum vessel, and were especially suited for the energy range 100–700 keV because of their dimensions of 47, 47, and 57 mm in diameter, all three being 26 mm deep. For higher energies, a larger GMX Ge detector was employed which had an efficiency of 17% at 1.33 MeV relative to the standard 3 in.$\times$3 in. NaI(Tl) detector. The Ge detectors were positioned as close as possible to the target vessel while allowing enough room for charged particle detectors V_1 and V_2 in front of them. The total solid angle covered by all Ge detectors was about 5% of 4π. In addition, during part of the experiment a neutron detector, capable of pulse-shape discrimination between neutrons and gammas, was placed below the target cell.

The primary experimental information was in the energies and in the times (with respect to the muon stop signal) of the signals in the two Ge detectors. The timing signals from both detectors were delayed by 1 μs, so that within the ''*event gate*'' the time range relative to the μ stop extended from -1 to $+4$ μs. Shortly after the end of the event gate, a coincidence logic decided whether the event was valid. Two conditions had to be fulfilled. First, only ''μ-real'' signals were accepted, these being μ-stop signals for which no second muon had been observed in detector S_1 for 4 μs before or afterwards. This pileup rejection eliminated ambiguities due to second muons impinging on the apparatus, and also reduced the accidental rate. Second, at least one Ge detector was required to have registered a photon within the event gate, while charged particles were vetoed by a prompt anticoincidence with detectors V_1 and V_2. In case the event met these criteria, the time (TDC) and energy [analog-to-digital converter (ADC)] information from the Ge detectors, the time information of the electron detectors V_1 and V_2, and finally the time, energy, and pulse-shape information from the neutron detector were recorded on magnetic tape via a microVAX-II computer. In addition, several counting rates were recorded by CAMAC scalers and read out in regular intervals. Some typical rates are given in Table II.

Background arose mostly from prompt stops in the Au coating on the plastic foils. This was measured by first filling the target with He of stopping power comparable to that at the highest pressure of H_2 or D_2 used in the actual data runs. It was found that the resulting time spectrum of Au signals with He was indistinguishable from that of the time spectrum obtained with the foil target evacuated, indicating that the stopping power of the gas in the target did not significantly affect the stopping distribution. Thereafter the background time spectrum was obtained by periodically accumulating data with the target chamber evacuated. Normalization of the vacuum background data was obtained by comparing muonic carbon x-ray intensities (generated in the plastic foils) with vacuum with those from H_2 or D_2. It is estimated that the normalization and subtraction of background introduced systematic errors of $<2\%$ into the final data, with negligible effect on the results of data analysis.

The Ge detectors provided most of the information needed for the diffusion time distributions. Outputs from other detectors were recorded in order to impose additional coincidence conditions on the Ge detectors so as to distinguish between muonic x rays from low-Z materials, where the probability for subsequent emission of decay electrons is high, and those in high-Z materials, which are usually followed by neutrons emitted in the nuclear capture process. Though this information proved helpful in identifying the origin of some x-ray lines, the high resolution of the Ge detectors for muonic x rays was sufficient to obtain very

TABLE II. Typical counting rates for the single-gap (0.23 cm) foil stack, a beam momentum $p_\mu=35$ MeV/c, and a proton beam current of ~ 225 μA at 590 MeV.

Scaler	Rate (10^3 s^{-1})
S_1	23.0
$S_1\cdot S_3$	17.2
μ stop	16.9
Event gate	13.3
μ real	9.2
Recorded events	0.76

clean signals associated with the diffusion process, so that the loss of statistics associated with the use of coincidence conditions was not justified.

If the event was not valid the ADC's and TDC's were cleared by a fast hardware signal, so that the system was ready for the next event after a few μs. The primary signal used for detection of the transfer to Au was the 356 keV nuclear γ ray emitted from Pt^{196} following nuclear capture of the transferred muon. A discussion of this choice was given in [5].

III. ANALYSIS OF DATA

The interpretation of the experiment depended upon analysis of the time distributions recorded under the various experimental conditions. An ''experimental condition'' was specified by (a) a target gas of either D_2 or H_2, along with (b) a gas pressure between 47 and 1520 mbar, and (c) foil gap of either 0.2286 or 0.4372 cm.

The ''time distributions'' were recorded as the number $N(t)$ of events between t and $t+\Delta t$, where t is the time between the incoming muon signal and a signal from one of the Ge detectors which is indicative of the formation of a muonic Au atom. The bin width Δt was chosen as a compromise between time resolution and the desirability of good statistical accuracy for the number of counts in each bin. Before analyzing the data they were all corrected for muon decay and subsequently dealt with as if generated by nondecaying muons.

A considerable amount of preprocessing of data was done to produce the time distributions [the electronic logic signal for an incoming muon was generated as described above in Sec. II B, and required no processing, since it was generated in standard CAMAC and NIM (nuclear instrumentation module) electronic logic hardware and provided a common trigger for the event]. The pulse-height spectra from the Ge detectors required fitting of all the peaks which were related to muon transfer from μp (μd) to Au. To fit the pulse-height spectra from the Ge detectors we used the program FIT 4.04 [9], which provided peak areas and widths with associated uncertainties, while taking into account the backgrounds in the neighborhood of each peak under the assumption that the background was locally linear. Real-time energy calibrations were provided by strategically located muonic x-ray lines, e.g., the 347-keV Kα line from muonic Al was conveniently near the nuclear γ-ray line at 356 keV from Pt^{196} which was the main indication of muonic Au formation in the target foils. The usual precautions were taken of frequent calibration checks of the muonic x-ray lines against radioactive sources, etc. to assure correct energy calibration for all detectors during data accumulation.

Since the time distributions form the primary results of the experiment, the calibration and measurement of circuitry response times was also essential. By studying the time (relative to the μ-stop signal) spectra of muonic x rays of various energies, it was possible to determine the [full width at half maximum (FWHM)] and shapes (in time) for the nuclear γ rays of interest. The various Ge detectors showed Gaussian time resolution functions with the width parameters σ measured to be 4.86 ns, 5.18 ns, 4.24 ns, and 4.56 ns for detectors A, B, C, and GMX, respectively, at 300 keV. Further, by

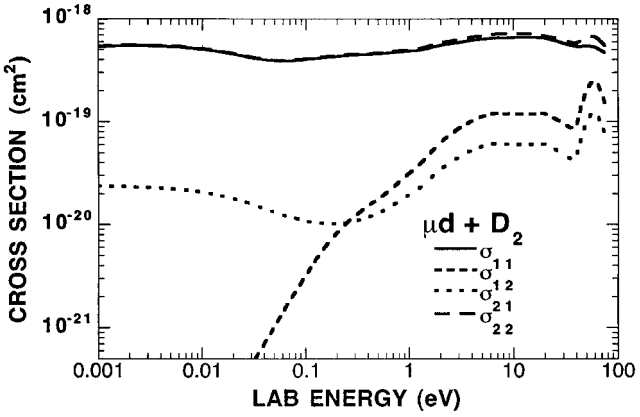

FIG. 2. Theoretical total scattering cross sections σ_{ij} for $\mu d+D_2$. Subscript i denotes the initial hyperfine state of the μd atom; j is the final state. Note that the elastic cross sections σ_{11} and σ_{22} in the two hyperfine states are almost equal below about 30 eV. All cross sections are averaged over the thermal motion of the D_2 molecule at 300 K.

stopping muons in a target of solid Au, we measured the mean life of muons in Au by means of the time spectra of the 356 keV nuclear γ rays from Pt^{196}. A mean life of 69.72 $\pm$0.14 ns was obtained, in fair agreement with the value quoted in the literature [10].

Up to this point we have been concerned with those characteristics of the detection apparatus which directly affect the time distributions generated from μp atoms striking the foil surfaces. There are, however, several physical quantities which also affect the time distributions, specifically the initial energy distributions of the μp and μd atoms, and the differential scattering cross sections vs energy for both types of atoms in both elastic and inelastic channels. These are not so readily measured. It is, in fact, the systematic comparison between the experimental time distributions and computer-generated time distributions concocted using various assumptions about these quantities, which gives experimental information about the physical quantities themselves. That information is currently not experimentally available except via the work reported here.

The accuracy to which any of the physical quantities, i.e., cross sections and energy distributions, can be determined is dependent on both the global nature and the quality of the data set. The present set includes a total of 324 data points spanning target pressures from 47 mbar to 1520 mbar (13 time distributions total). Having data for both hydrogen and deuterium is of importance, first because the energy dependence of the theoretical scattering cross sections for μp and μd are quite different (see Figs. 2 and 3), which could be tested by analysis of the data. Second, it appears that at the lowest pressures used in this experiment the time distributions for μp and μd are strikingly similar if the time scale for μd is altered by a factor of 2 in such a way that the μd's appear to have their velocities doubled (Fig. 4). This suggests that at these pressures the μd and μp possess the same functional form of initial energy distribution, and that the μd distribution is a factor of 2 lower in mean velocity (and thus in energy) than the μp distribution.

In making the comparison between the experimental and computer-generated time distributions, it is necessary to be

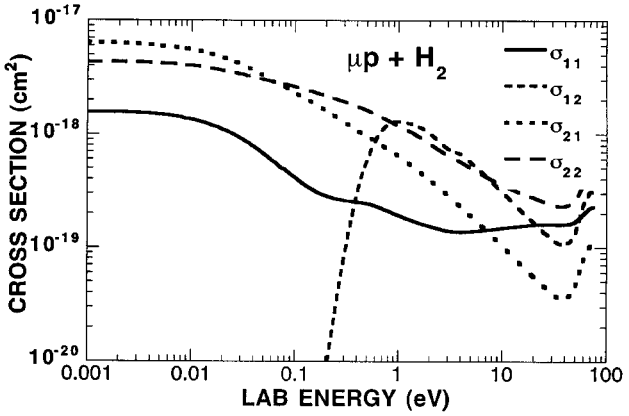

FIG. 3. Theoretical total scattering cross sections σ_{ij} for $\mu p + H_2$. Subscript i denotes the initial hyperfine state of the μp atom; j is the final state. Note that the elastic cross section σ_{22} in the upper hyperfine state is 4–10 times larger than σ_{11} in the lower state for energies up to about 10 eV. All cross sections are averaged over the thermal motion of the H_2 molecule at 300 K.

able to develop by computer a large number of time distributions, in fact a multidimensional grid of time distributions, using various assumptions about scattering and initial kinetic energy distribution for the experimental condition. The experimental time distributions can then be compared with the grid, using the least squares method to derive from the computed grid that hypothetical time distribution which best approximates a particular experimental time distribution.

In standard fashion the computed time distributions were generated by a Monte Carlo (MC) method. To accomplish this, a MC simulation of the muonic atom diffusion and subsequent capture on the gold foils was performed. The simulation begins after atomic capture of the muon and completion of the cascade process through which the μp or μd reaches the ground $1S$ states. The nature of the cascade process and the shape of the experimental apparatus lead to certain initial assumptions for the muonic atoms. First, the diffuseness of the incoming muon beam and the geometry of the stacked foil structure, as well as the characteristics of muons slowing down in matter, are assumed to provide a uniform distribution of muonic atoms forming between foils and throughout the radius of the target chamber (cf. Sec. II). Second, the nature of the muon capture and cascade processes indicates that upon reaching the ground state the muonic hydrogen atom's direction of motion will be isotropic, the muon having lost all knowledge of its momentum direction since the instant of capture. And finally, due to depolarization during the atomic cascade, the initial hyperfine states of the ground-state muonic atoms are expected to be populated in the statistical ratios (though there is no experimental proof of this known to the authors). For the μp atom the possible hyperfine states are $F=0,1$ and for the μd atom $F=\frac{1}{2},\frac{3}{2}$. Knowledge of the initial hyperfine state population is important because the scattering cross sections depend on the hyperfine state, this sensitivity being particularly strong for $\mu p + H_2$ scattering.

A Monte Carlo code called MCGRID was developed over an extended period in order to simulate the histories of muonic hydrogen atoms in the parent gases in various cylindrically symmetric target geometries and at arbitrary pressure. The program has been altered to take account of the availability of newly refined theoretical scattering cross section calculations [6] (cf. Sec. IV for a discussion of the cross section theory). Early MCGRID versions used scaled (doubled for molecules) nuclear cross sections ($\mu p + p$ and $\mu d + d$) in the s-wave approximation, which proved to be inadequate to describe the data, in the sense that the use of such cross sections always resulted in least squares fits to the data which had high values of χ^2, i.e., were statistically improbable. Thus it appeared that higher partial waves in the nuclear cross sections plus such molecular effects as excitation of rotational states and electron screening were important to the microscopic description of the diffusion process.

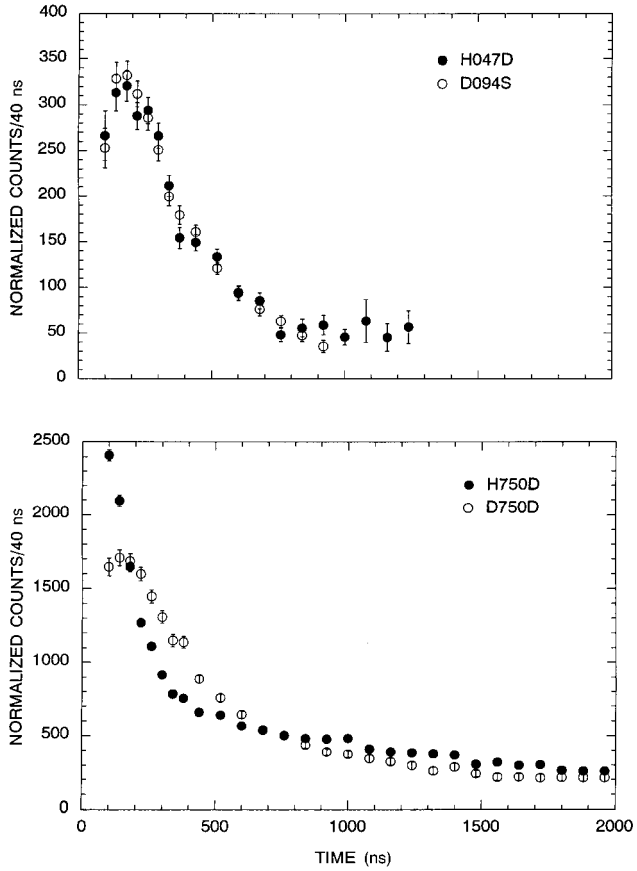

FIG. 4. Experimental data for (top) low pressures of D_2 (D094S denotes D_2 target at 94 mbar and 0.23 cm foil spacing) and H_2 (H047D is H_2 target at 0.46 cm foil spacing), and (bottom) high pressure of D_2 and H_2. Note that the μp (triangle symbols) traverse twice the foil spacing as the μd atoms (circle symbols) in the upper graph. In the lower graph the effect of scattering has been to distort the μd relative to the μp curves, both with the same foil aperture.

The cross section input for MCGRID is provided for $\mu p + H_2$ and $\mu d + D_2$ in the form of four differential cross sections as a function of E, the laboratory kinetic energy of the diffusing atom:

$$\frac{\partial^2 \sigma_{11}^{\mathrm{mol}}}{\partial E_f \partial \theta}(E,E_f,\theta), \quad \frac{\partial^2 \sigma_{12}^{\mathrm{mol}}}{\partial E_f \partial \theta}(E,E_f,\theta), \tag{1a}$$

$$\frac{\partial^2 \sigma_{21}^{\mathrm{mol}}}{\partial E_f \partial \theta}(E,E_f,\theta), \quad \frac{\partial^2 \sigma_{22}^{\mathrm{mol}}}{\partial E_f \partial \theta}(E,E_f,\theta). \tag{1b}$$

E_f is the final laboratory energy of the scattered atom and θ is the laboratory scattering angle. The subscripts 1,2 refer to the lower and upper hyperfine states, respectively. The four molecular cross sections represent ''elastic'' ($\sigma_{11}^{\rm mol}$ and $\sigma_{22}^{\rm mol}$) and spin-flip ($\sigma_{12}^{\rm mol}$ and $\sigma_{21}^{\rm mol}$) quantities and have been calculated for 100 values of E between 0.001 eV and 75 eV. Cross section values needed by MCGRID, but not explicitly calculated, are interpolated from the input data set via a spline fit. These cross sections have taken into consideration both s- and p-wave scattering, molecular effects including rotational and vibrational transitions, spin correlations, electron screening, and Maxwell averaging over the room temperature distribution of the target gas (see Sec. IVB below). We have also incorporated a scaling parameter ($\mathcal{F}$) which can be allowed to vary so as to simultaneously adjust the normalization of all cross sections, i.e., $\mathcal{F}$ is a scale factor which is independent of energy. If the assumed theoretical cross sections were in fact physically correct, then the least squares fit to the data would yield a $\mathcal{F}$ equal to 1.0 .

The cross sections are used within MCGRID in three different ways. First, the differential cross sections are read in and integrated over both final energy and angle, giving total cross sections as a function of laboratory energy. These cross sections are used to determine the mean free path for collisions between muonic atoms and the target gas. Once a point of collision has been determined, the total cross sections are again used to determine whether a hyperfine spin-flip transition has occurred. Finally, the partial differential cross sections are used to find a final laboratory energy and trajectory for the scattered muonic atom. This procedure is looped through for each diffusing atom until it reaches one of the gold foils or is lost to the sidewalls. Also included are the effects of processes such as backscattering from foils, timing resolution of the detectors, nuclear capture on gold, and loss of low-energy events due to capture on thin carbon layers covering the gold surface.

The final input to MCGRID is the initial energy distribution for the diffusing muonic atoms as they reach the ground state. Understanding the nature of this distribution is a primary goal of this analysis. Thus a method within MCGRID is used for parametrizing the initial energy distribution and then performing multiple diffusion calculations for a range of parameter values. This gives us a ''grid'' of Monte Carlo time distributions from which the best values of the parameters are found through a global fitting procedure with the experimental time distributions. The CERN code MINUIT is used in the least squares fitting analysis, as it provides as output a quantitative measure of the confidence limits for a given set of parameter values.

Detailed theoretical predictions for the structure of the initial energy distribution are currently not available [11], and it is in any case unlikely that the energy distribution can be exactly described analytically. However, the computation of a multidimensional grid of Monte Carlo time distributions requires that each time distribution will be characterized by values for a finite number of parameters. Therefore it is necessary in preparing the grid to assume initial energy distributions which can be described by functions involving a reasonable number of parameters (here limited to 3). Thus the goal is to describe this distribution empirically, in order to have a way of accurately predicting the diffusion process within the range of the complete data set. We have concentrated on using only a few initial energy distribution functions, used both individually and in combinations, in an attempt to simulate the data, and we have observed that some of these analytical energy distributions give time distributions which are quite similar to the experimental time distributions. They are the delta-function $\delta(E)$, the Maxwell $M(E)$, the Gaussian $G(E)$, the power $P(E;\alpha)$, and the rectangular distribution $S(E)$. The power distribution is defined by the following formula:

$$\mathrm{P}(E;\alpha)=\frac{(1-\alpha)^{2-\alpha}}{(2-\alpha)^{1-\alpha}}\frac{E^{-\alpha}}{\langle E\rangle^{1-\alpha}},\quad E_1\leqslant E\leqslant E_2 \tag{2a}$$

$$E_1=0.001\ \text{eV},\quad E_2=\frac{2-\alpha}{1-\alpha}\langle E\rangle, \tag{2b}$$

where $\langle E\rangle$ is the mean muonic atom energy. Frequently used combinations such as the double Maxwell ($\mathcal{M}_D$)

$$\mathcal{M}_{\mathcal{D}}(E;f)=(1-f)M_{\rm th}(E)+fM(E),\quad 0\leqslant f\leqslant 1 \tag{3}$$

where $M_{\rm th}$ is the Maxwell distribution corresponding to the thermal energy of 0.04 eV, the power$+\delta$ (PD), Maxwell $+\delta$ (MD), and the three-component distribution ($3C$) $[=M1(E)+M2(E)+\delta(E)]$ will also be referenced throughout this discussion.

A. Deuterium analysis

As was discussed above, the nature of the scattering cross sections for hydrogen and deuterium must affect the time distributions observed with these two target gases. For deuterium, $\mu d+\mathrm{D}_2$, the total cross sections are relatively flat functions of energy, and are virtually identical for the doublet (σ_{11}) and quartet (σ_{22}) elastic scattering. In addition, the spin-flip total cross sections (σ_{12},σ_{21}) are relatively small with respect to the elastic ones. Hence the diffusion process in D_2 at a specified μd kinetic energy is relatively insensitive to the hyperfine state. However, it was found important to include the p-wave component to the scattering amplitudes for μd even at collision energies below 1 eV.

In the deuterium data set there are eight time distributions, corresponding to five single-gap pressure conditions and three double-gap conditions. All time distributions were binned in 40 ns intervals for times $\leqslant$400 ns and then in 80 ns bins for times out to 2 μs. This was to ensure good statistics for each bin when fitting to the parametrized energy distributions for the diffusing atoms. In general, fitting of the experimental time distributions required an iterative procedure of creating a coarse grid of low statistics Monte Carlo distributions with MCGRID and then determining the appropriate range of parameters (such as mean energy, $\mathcal{F}$), and then generating a finer mesh high statistics grid around these values. A ''high statistics'' grid involved at least 40 000 events per mesh point, which is to be compared with 6000–7000 or fewer events in each experimental time distribution. The high statistics grids were in turn used with MINUIT to obtain the best fit to the experimental data.

The determination of an appropriate initial energy distribution for the μd atoms was somewhat *ad hoc*. It was instructive to look at some energy distributions which were

TABLE III. MINUIT fit to $\mu d+D_2$ experimental diffusion time distribution using a power initial energy distribution $P(E;\alpha)$. In the individual fits the molecular factor $\mathcal{F}$ was allowed to vary for each condition. For the free energy fits the $\mathcal{F}$ was constrained to have the same value for all conditions. Where calculated, error limits are for one statistical standard deviation as computed via MINOS. For free pressure fits the $\mathcal{F}$ was the same for all fits, and E was constrained to be the same for both single (0.23 cm) foil gap conditions and double (0.23 cm) foil gap conditions at the same pressure; e.g., D375S and D375D conditions. The notation for conditions is, e.g., D094S$\equiv D_2$ target gas, 94 mbar pressure, single foil gaps. The values of α are also given for this two-parameter distribution. DOF denotes degrees of freedom.

Condition	Mean energy (eV)	α	$\mathcal{F}$	DOF	Reduced χ^2
		Individual fits			
D094S	1.21	0.21	1.45	12	0.66
D188S	1.44	0.38	1.00	17	0.54
D375S	2.00	0.51	1.06	20	0.51
D750S	2.21	0.61	0.82	25	0.93
D1520S	2.85	0.49	0.97	25	1.02
D188D	2.00	0.68	1.03	22	0.99
D375D	1.99	0.78	0.65	25	1.05
D750D	3.18	0.76	0.63	25	0.41
		Free energy fits			
D094S	$1.17+0.50-0.35$	$0.20+0.60-0.00$ [a]			
D188S	$1.44+0.38-0.27$	$0.42+0.24-0.22$			
D375S	$1.96+0.32-0.48$	$0.52+0.12-0.12$			
D750S	$2.20+0.77-0.49$	$0.52+0.11-0.11$	$0.97+0.13-0.13$	178	0.90
D1520S	$2.85+1.15-0.87$	$0.50+0.30-0.30$			
D188D	$2.01+0.58-0.58$	$0.68+0.12-0.13$			
D375D	$2.07+0.62-0.44$	$0.55+0.16-0.16$			
D750D	$2.85+0.84-0.85$	$0.53+0.16-0.16$			
		Free pressure fits			
D094	$1.17+0.66-0.26$	$0.20+0.48-0.00$[a]			
D188	$1.69+0.36-0.27$	$0.47+0.22-0.27$			
D375	$2.02+0.15-0.15$	$0.52+0.08-0.08$	$1.01+0.07-0.07$	184	1.01
D750	$2.70+0.16-0.14$	$0.58+0.05-0.05$			
D1520	$2.84+1.16-0.53$	$0.49+0.08-0.25$			

[a]Parameter is at the fixed low limit of 0.20.

simple in form, but which did not fit the experimental data particularly well. These are the δ-function and Maxwell distributions, both having the convenient property of being defined by a single parameter. In these two cases, however, there were actually two free parameters used — the mean energy $\langle E\rangle$ of the initial distribution and the $\mathcal{F}$ scaling factor for the cross sections (cf. above). We defined three types of least squares fits to the data. The first was the ''individual'' fit, which was composed of independent fits to each of the eight time distributions, thus allowing a determination of the ''best-fit'' parameters $(\langle E\rangle_i,\mathcal{F}_i)$ for each condition. Using a δ-function form for the initial energy distribution yielded values for reduced χ^2 which were large (≈ 2), as well as $\mathcal{F}$ values also ≈ 2 at the lower pressures. For the Maxwell distribution the quality of fits was better, though the $\mathcal{F}$ often took on values exceeding 1.2. (The $\mathcal{F}$ could change from its ideal value of 1.0, corresponding to agreement with the theoretical cross sections, as MINUIT attempted to compensate for an inadequate initial energy distribution.) For both types of distribution there appeared to be an increase in $\langle E\rangle$ with increasing pressure. Two other types of fit defined for this analysis were the ''free energy'' and ''free pressure'' fits. For the free energy fit we made the restriction that $\mathcal{F}$ be the same for all conditions. For the free pressure fit we made the additional restriction that for a given pressure the single- and double-gap results must have identical initial energy distributions. The results of these fits for the δ-function and Maxwell distribution showed the Maxwell to be superior to the δ, indicating the need for a broad distribution in energy, but the reduced χ^2 were still not satisfactory.

B. Thermal components

After a muon has been captured on a deuterium molecule to form a μd atom, it is expected [12] that during the cascade process there is significant probability that the μd atom will be thermalized. Therefore we have considered some initial energy distributions which include a thermal component (mean energy 0.04 eV) of variable fractional area, the total area always being normalized to unity. The two distributions most readily parametrized for this investigation were the

TABLE IV. MINUIT fit to $\mu d + D_2$ experimental diffusion time distribution using a double Maxwell initial energy distribution $\mathcal{M}_D(E;f)$. See caption for Table III, except that here energy E is the mean energy of the higher-energy Maxwell component in the $\mathcal{M}_D$ distribution, and f is the fraction of total area in the high-energy Maxwell. The low-energy Maxwell has a thermal energy of 0.04 eV.

Condition	Mean energy (eV)	f	$\mathcal{F}$	DOF	Reduced χ^2
		Individual fits			
D094S	1.29	0.90	0.82	12	0.75
D188S	1.75	0.82	0.81	17	0.48
D375S	2.08	0.96	1.43	20	0.66
D750S	2.48	0.83	0.91	25	1.01
D1520S	2.52	1.00[a]	1.12	25	0.90
D188D	2.60	0.70	1.02	22	0.95
D375D	2.42	0.86	1.11	25	1.21
D750D	3.79	0.70	0.65	25	0.51
		Free energy fits			
D094S	$1.33+0.87-0.44$	$0.88+0.12-0.33$			
D188S	$1.76+0.67-0.43$	$0.83+0.17-0.17$			
D375S	$2.12+0.70-0.47$	$0.85+0.15-0.14$			
D750S	$2.46+0.75-0.41$	$0.84+0.10-0.10$	$0.92+0.10-0.10$	178	0.89
D1520S	$2.83+1.17-0.41$	$0.87+0.09-0.13$			
D188D	$2.69+1.24-0.99$	$0.66+0.34-0.20$			
D375D	$2.72+1.18-0.86$	$0.74+0.26-0.19$			
D750D	$3.69+0.30-1.62$	$0.81+0.19-0.15$			
		Free pressure fits			
D094	$1.33+0.54-0.45$	$0.88+0.12-0.12$			
D188	$2.15+0.52-0.18$	$0.74+0.07-0.13$			
D375	$2.41+0.21-0.29$	$0.79+0.08-0.05$	$0.92+0.06-0.06$	184	1.12
D750	$3.00+0.99-0.15$	$0.81+0.09-0.09$			
D1520	$2.83+0.74-0.18$	$0.87+0.09-0.09$			

[a]Parameter is at the fixed high limit of 1.00.

''power'' distribution ($E^{-\alpha}$), in which α can be varied to adjust the proportion at lower energies,[1] and the ''double Maxwell,'' where one Maxwell component is fixed to a mean energy of 0.04 eV and the other is allowed to have a variable energy to optimize the least squares fit. In both cases the parameter corresponding to the fraction of the thermal component could be varied. Both distributions have two parameters associated with the energy distribution in addition to the $\mathcal{F}$ parameter. Fits (for μd) for both parametrizations showed that for every condition the individual fits for both distributions yielded good χ^2. After adding the single $\mathcal{F}$ restriction for the free energy fit, the quality of the fit was still satisfactory. At this point the addition of the free pressure restriction forcing single- and double-gap energy distributions to be the same was interesting in that the double Maxwell fit worsened while the power fit was still quantitatively good. These results are shown in Tables III and IV. The question of evidence for a thermal component to the energy distribution can be studied from these fits. First, the addition of a thermal component to the single Maxwell distribution clearly improved the fit at all pressures and spacings. The fraction of thermal component, however, was relatively constant at around 15–20 % for all pressures, though increasing pressure was expected to increase the thermal fraction. Similarly, for the power distribution the fraction of the low-energy component stayed relatively constant (i.e., $\alpha \sim 0.5$) for all pressures except the D094S case, where an $\alpha \sim 0.2$ indicates a smaller low-energy fraction.

The first thing to note about the individual fits for both distributions is that for every condition good χ^2 are obtained. By adding the single $\mathcal{F}$ restriction for the free energy fit, one sees that the quality of the fit is still satisfactory, with reduced χ^2 for both cases being less than 1.0 and the best-fit $\mathcal{F}$ being very close to 1.0.

C. High-energy components

While the mean energy of muonic or pionic atoms when initially formed is expected to be of the order of eV, evidence exists for the presence of a ''high-energy'' component with energy of 50–100 eV for *pionic* atoms formed in liquid and gaseous H_2 [13,14]. This component has been observed at the time of nuclear absorption of the pion by the proton, the absorption being estimated to occur mainly from the $n=3,4$ S state. The high-energy component is thought to develop through acceleration of the pionic atom during collisions with hydrogen molecules by a process of Coulomb deexcitation of the pionic atom. In such processes the pionic atom can acquire recoil kinetic energy, in contrast with radiative deexcitation in which the photon takes away the transition energy. This process would also be expected to apply

[1]The mean energy $\langle E \rangle$ is also an adjustable parameter. Specifying both α and $\langle E \rangle$ fixes the upper cutoff energy of the power distribution — the lower cutoff is 0.001 eV.

to μp and μd atoms. Markushin [11] has developed the theory of the high-energy components for μp and μd in H_2 and D_2 gas at pressures similar to those used in the experiment reported here.

Since an analysis of our data already showed an increase in mean energy vs pressure for all experimental initial distributions, even the simple δ-function and Maxwell forms (cf. above), it was appropriate to study more carefully the possibility of a ''high-energy'' component. One issue concerned the degree to which our experimental setup was sensitive to high-energy components. For example, the perpendicular transit time for a 1-eV μp atom crossing the 0.23 cm foil gap is 180 ns, whereas the rise time of the detection system is approximately 70 ns. Thus the detection system cannot be expected to be able to distinguish among muonic atom energies exceeding about 20 eV, though it will be sensitive to the presence of such high-energy components. Tests confirmed that it was difficult to distinguish between time distributions generated from muonic atoms with a mean energy of 25 eV and those with 50 eV or more. Therefore we chose to make tests of high-energy components by adding a δ-function distribution with energy E_δ to another primary distribution such as a Maxwell, double Maxwell, or power. The computational load of generating Monte Carlo grids with many free parameters became a serious problem during the fitting process with these energy distributions. Thus it was decided, given the consistency of the $\mathcal{F}$ parameter with 1.0 (no cross section scaling) during tests of simpler distributions, and also because the theoretical calculations were expected to be accurate only within 5–10 %, to fix this parameter at 1.0 in order to allow the introduction of energy distributions involving more free parameters. In effect, the ''individual'' fit cases were eliminated during this part of the analysis.

Results of high-energy component tests for μd diffusion were in general inconclusive. Acceptable fits could be found without the presence of such a component; its inclusion generated equally good or slightly improved fits to all time distributions. However, we were unable to accurately determine the magnitude or the mean energy of this component. E_δ ranged from 10 eV up to 25 eV and ranged in magnitude from 0 to 30%. In both the power+δ and the three-component (thermal+Maxwell+δ) fits, neither of these quantities showed any clear correlation with pressure. Thus there did not seem sufficient justification to choose these distributions rather than their simpler counterparts. It is important to note, however, that analysis of this experiment finds no disagreement with Markushin's [11] predictions, which estimate the high-energy component ($E>8$ eV) for the conditions of the present experiment to reach a maximum about 30% at 1.5 bars. Moreover, an increase in mean energy of the μp and μd atoms with gas pressure is experimentally established in this experiment.

D. Hydrogen analysis

As was pointed out previously, understanding the kinetics of the muonic hydrogen diffusion is made complicated by the structure of the cross sections, which differ in several ways from muonic deuterium cross sections. First, the μd cross sections are relatively constant over the energy range of interest (0–100 eV), while the μp cross sections change by almost two orders of magnitude. In addition, the two hyperfine state cross sections, while virtually identical for μd, differ by a factor of 2–10 for μp over the same energy range. Finally, the μp spin-flip cross sections are of the same magnitude as or larger than the elastic cross sections. This last feature, coupled with the large cross section difference between singlet and triplet states, leads to a situation in which some diffusion time distributions can be very sensitive to all the various input parameters such as the initial energy distribution, as well as the initial hyperfine state population distribution.

The size of the hyperfine splitting is also greater for μp (0.182 eV) than for μd (0.0485 eV). The latter is scarcely larger than the thermal energy of 0.04 eV at 300 K, and so it has little effect on hyperfine population even for thermalized μd atoms. On the other hand, μp atoms with laboratory kinetic energies of 0.2–0.4 eV are beginning to move irreversibly into the singlet state as scattering further reduces the

TABLE V. MINUIT fit to $\mu p+H_2$ experimental diffusion time distribution using a power initial energy distribution $P(E;\alpha)$. See caption for Table III, except that here there are no free pressure fits because only one foil spacing was used.

Condition	Mean energy (eV)	α	$\mathcal{F}$	DOF	Reduced χ^2
		Individual fits			
H047D	2.08	0.50	0.60[a]	16	1.58
H094D	3.76	0.66	0.60[a]	25	2.49
H188D	4.49	0.70	0.66	24	1.88
H375D	6.65	0.80[b]	0.83	24	1.85
H750D	8.02	0.79	0.81	25	2.21
		Free energy fits			
H047D	2.14+0.56−0.56	0.49+0.15−0.15			
H094D	3.75+0.57−0.57	0.64+0.08−0.08			
H188D	4.51+0.28−0.28	0.69+0.06−0.06	0.72+0.05−0.05	118	2.12
H375D	6.09+0.46−0.46	0.80+0.00−0.03[b]			
H750D	6.84+0.41−0.41	0.80+0.00−0.04[b]			

[a]Parameter is at the fixed low limit of 0.60.

[b]Parameter is at the fixed high limit of 0.80.

TABLE VI. MINUIT fit to $\mu p + H_2$ experimental diffusion time distribution using a double Maxwell initial energy distribution $\mathcal{M}_D(E;f)$. See caption for Table IV; there are no free pressure fits here.

Condition	Mean energy (eV)	f		$\mathcal{F}$	DOF	Reduced χ^2
		Individual fits				
H047D	2.56	0.85	1.11	16	1.59	
H094D	3.60	0.97	1.40	25	2.56	
H188D	6.75	0.68	0.78	24	1.40	
H375D	12.57	0.51	0.75	24	1.20	
H750D	16.04	0.50	0.78	25	1.83	
		Free energy fits				
H047D	$2.57+1.21-0.65$	$0.81+0.19-0.24$				
H094D	$4.07+1.25-0.54$	$0.81+0.06-0.11$				
H188D	$6.75+0.80-1.68$	$0.68+0.10-0.04$	$0.78+0.05-0.10$	118	1.77	
H375D	$16.08+2.29-5.25$	$0.47+0.04-0.03$				
H750D	16.02[a]	$0.50+0.04-0.03$				

[a]Parameter limits were so close to the computed value that MINOS did not yield reliable results for the errors.

kinetic energy. Since the singlet μp scattering cross section is considerably smaller than the triplet one for these energies, the singlets will move more rapidly than the triplets through the target gas to the Au-coated foil surfaces. This effect is manifest in the structure of the higher-pressure diffusion time distributions, for which scattering (and hence thermalization) is dominant. One notes the difference in shape between the μp and μd time distributions in Fig. 4, with a strong decrease in the rate at early times followed by ''leveling off'' after about 400 ns in the μp.

The analysis for the μp diffusion distributions followed much the same course as for the μd distributions, with many initial energy distribution functions tried. The fit types were the same with the exception of the ''free pressure'' case, which could not be made as there were only double-gap μp data. Also for the μp data there were five time distributions acquired at pressures ranging from 47 mbar to 750 mbar. The final results for the ''individual'' and ''free energy'' fits for the power and double Maxwell distributions are listed in Tables V and VI.

There are some striking differences between the μp and μd fits. First, the overall χ^2 values for all fits are substantially worse for the μp, and also no individual μp distribution is fitted well. In addition, there is a systematic trend towards poorer fits with increasing pressure.[2] Turning to the power and double Maxwell parametrizations, which fitted well in the μd case, we see that for μp the fits are poor for both the individual and free energy fits. The pressure correlation of $\mathcal{F}$ is significantly reduced, and it has stabilized around 0.8. But unlike the μd case, the double Maxwell fit clearly distinguishes itself from the power as the better parametrization. This seems primarily due to its ability to distinguish between a thermal component, which increases with increasing pressure, and a higher-energy component.

In all μp fits the pressure dependence of mean energy is much stronger than for the μd case, and for the DM fit this is particularly true. This is somewhat troubling because of the strong cross section dependence with energy that exists. If there were some inaccuracy in the cross sections, it would manifest itself in either increasingly poor fits with pressure or a strong mean energy dependence with pressure of the initial distribution, or both. If it is assumed that the μp and μd initial energy distributions are of similar form (but have different mean energies, for example), the above problems suggest the possibility of error in theoretical cross sections upon which the fitting procedure is based. In this connection we note that independent of the form chosen for the initial energy distribution, at higher pressures the μp $\mathcal{F}$ moves to 0.9 ± 0.1, suggesting that any inaccuracy in the cross sections is not associated with overall normalization through the relevant energy region, but rather on the detailed behavior of the cross sections over a restricted energy range.

To test these ideas, a fit was made in which the $\mathcal{F}$ was allowed to have its apparently preferred value of 0.8 over all energies for the triplet only, while the singlet $\mathcal{F}$ was allowed to float. The MINUIT least squares fit then chose a singlet $\mathcal{F}$ of 2.0, with reduced mean energy, for a somewhat improved fit. This test was made only to demonstrate that a particular change in cross sections can improve the fits to the experimental time distributions, especially those at higher pressures, which are more sensitive to scattering than to the initial energy distribution of the μp atoms. Considerably more experimental data would be necessary to deduce details of the energy and angular dependence of the four cross sections involved, and with the present data it is possible only to test the theoretical cross sections by seeing whether they provide a good fit to the data, especially for high-pressure conditions.

Some of the points mentioned above in Sec. III are illustrated in Fig. 5, which shows both the experimental data (points with errors bars) and fits (continuous and dashed lines) for two conditions: 375 mbar D_2 with single (0.23 cm) spacing, and 375 mbar H_2 with double (0.46 cm) spacing. In each case we see (a) a peak at early arrival times at a foil, and (b) a long tail extending out to where the number of events becomes statistically useless (we used signal equal to

[2]The case of the 94-mbar pressure and double foil spacing is an exception to this statement. However, this condition was seen to have considerably worse fits primarily due to poor data quality from scatter inconsistent with the uncertainties assigned. Some as yet undiscovered systematic errors for this condition may be the cause.

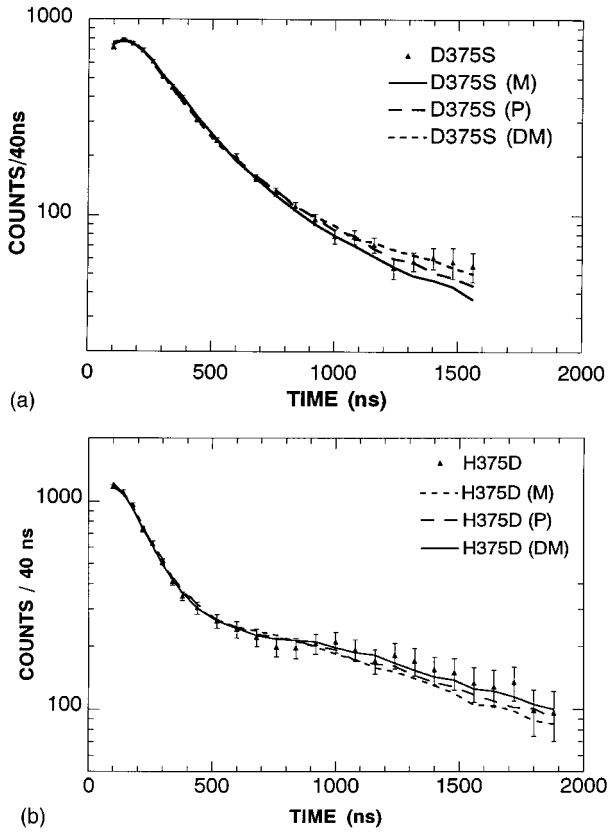

FIG. 5. Experimental data and Monte Carlo ''free pressure'' fits for $\mu d + D_2$ at 375 mbar with foil spacing of 0.23 cm (top), and ''free energy'' fits for $\mu p + H_2$ at 375 mbar with foil spacing of 0.46 cm (bottom). The Monte Carlo fits are to the best (minimum χ^2) energy distributions of the Maxwell (M), power (P), and double Maxwell (DM) forms. Characteristics of these Monte Carlo fits, which are seen for all conditions, are evident in the two cases displayed here; e.g., the Maxwell fit is always the worst among the three types shown. Also the μd time distribution always shows a steady decline with time, while at pressures of 200 mbar and above the μp data exhibit a plateau from 500 to 1000 ns.

background as criterion for the data cutoff at long times). We note that the H_2 data appear to have a plateau at 500–1000 ns; the D_2 data just decline steadily with time. As for the fits, the single Maxwell is worst; for both H_2 and D_2 the double Maxwell distribution appears best. The poorer quality of fit for H_2 as compared to D_2 is not apparent for these two conditions; it is our impression that overall the H_2 fits are worst in the neighborhood of 500–1000 ns for the higher-pressure (188–750 mbar) conditions.

IV. THEORETICAL ASPECTS OF SCATTERING OF MUONIC ATOMS

A. Scattering from nuclei

In describing the scattering of muonic atoms in a mixture of hydrogen isotopes it is necessary to solve the three-body Coulomb problem in the continuum. In the first approach we neglect the effects of electron screening and molecular bonds (which seems reasonable because the muon Bohr radius a_μ is much smaller than the electron Bohr radius a_e: $a_\mu/a_e = m_e/m_\mu \sim 1/200$), then the problem is one involving three Coulombic particles of comparable mass, namely, the nucleus a, the muon which is bound to nucleus a to form the muonic atom μa, and finally the nucleus b which scatters μa.

The channels for low-energy collisions of muonic atoms with nuclei of hydrogen isotopes are

$$\mu a + b \rightarrow \mu a + b, \quad \text{elastic scattering,} \tag{4a}$$

$$\mu a + b \rightarrow \mu b + a, \quad \text{isotope exchange,} \tag{4b}$$

$$(\mu a)_F + a \rightarrow (\mu a)_{F'} + a, \quad \text{spin flip } F \rightarrow F'. \tag{4c}$$

We note that in contrast with conventional atomic collisions, in these muonic atom processes a small parameter corresponding to $m_e/M \sim 10^{-3}$ is absent (here M is the reduced mass of the nuclei). As a result, nonadiabatic effects are important here, because $m_\mu/M \sim 10^{-1}$. Taking these effects into consideration is quite complicated, and has required further development of the conventional methods of atomic physics. Thus far the most accurate and complete results have been obtained by extending the Born-Oppenheimer approximation with the method of perturbed stationary states (PSS) as applied in atomic physics to muonic atom scattering, in order to include the effects of nonadiabaticity. The idea of this approach (also referred to as the adiabatic representation in the Coulomb three-body problem) is to expand the three-body wave function in terms of the basis functions of the two-center problem [15]. Most of the attempts have been made in a framework of the two-level adiabatic approximation, i.e., taking into consideration only the two lowest states of the basis set. Such calculations had their beginnings in Refs. [16,17]. The incomplete inclusion of the nonadiabatic motion of nuclei made in the two-level approximation [18,19] has a significant effect. In the paper [20] a simple recipe was suggested to improve the two-level PSS approximation by correcting the effective masses in the various channels. It was shown [21] that such improvement of the approach, i.e., more precise treatment of the nonadiabatic effects, may dramatically change scattering cross sections in some cases. The scattering cross sections σ_{ij} and corresponding reaction matrices for muonic hydrogen atoms scattered by hydrogen isotopes have been calculated by this approach in a broad CMS collision energy range (0.001 eV $\leqslant \varepsilon \leqslant$ 50 eV) [22].

Other attempts to improve the two-level PSS approximation have been made by Kobayashi *et al.* [23], who applied two sets of Jacobi coordinates, which leads to separate sets of adiabatic states in each channel, and by Cohen and Struensee [24], who used the two lowest states of the ''improved'' adiabatic basis [25].

The extension of the PSS approach to the multichannel scattering problem has been done in the papers [26,27]. This permitted testing of the convergence of the multichannel adiabatic method in the problem of muonic atom scattering by the nuclei of hydrogen isotopes, and also the calculation of these cross sections with controlled accuracy. This approach has been successfully applied to all combinations

of hydrogen isotopes for all processes happening during the deceleration of a ground-state muonic atom from about 100 eV to 0.001 eV, including elastic scattering, isotope exchange, hyperfine transitions, and the ''in flight'' fusion reaction. The results have been published as an atlas of scattering cross sections (and the corresponding reaction matrices) for the energy range $0.001\ \text{eV} \leqslant \varepsilon \leqslant 100\ \text{eV}$ [28,29]. The accuracy achieved here for the calculated cross sections is a few percent. This estimation has been confirmed recently at zero collision energies for the reactions $\mu p + p \rightarrow \mu p + p$ and $\mu d + d \rightarrow \mu d + d$ by solving numerically the Fadeev equation [30,31]. The agreement of the calculated scattering lengths with the multichannel adiabatic results [28] are within 2% for the $\mu p + p$ case and 2–3 % for $\mu d + d$. We also mention two other multilevel results obtained so far: variational [32], based on the use of a Gaussian basis set, and hyperspherical [33] calculations of the exchange rate $\mu d + t \rightarrow \mu t + d$, both giving results close to the multilevel PSS (see [34]). We note that among existing two-level results, those of Ref. [22] are closest to the multichannel calculations [28] for symmetric collisions $(\mu a)_F + a \rightarrow (\mu a)_{F'} + a$. The scattering cross sections differ less than 10–20 %, and for some energy regions the agreement is as good as a few percent.

B. Scattering from molecules

In the experiments discussed here one actually deals with gaseous *molecular* hydrogen and deuterium targets. Therefore it is necessary to take into account the effects of molecular binding and electron screening, as discussed below.

The screening effects turn out to be important for elastic scattering at collision energies below about 1 eV [35–37]. The cross sections for the scattering of muonic hydrogen on hydrogen molecules (''molecular'' cross sections) used in our Monte Carlo simulations were calculated using an effective screening potential. This potential is obtained in the second order of perturbation theory with respect to the small parameter $\sqrt{m_e/m_\mu} \approx \frac{1}{14}$. In the case of the hydrogen molecule, the potential takes the following form [38] in the muonic atomic units ($\hbar = e = m_\mu = 1$):

$$\begin{aligned} V_e(\mathbf{r}_a, \mathbf{r}_b, \mathbf{r}_c) = -C\{&\exp(-2.4|\mathbf{r} + \tfrac{1}{2}\mathbf{R}|/a_e) \\ &+ 1.35\exp[-1.2(|\mathbf{r} + \tfrac{1}{2}\mathbf{R}| + |\mathbf{r} - \tfrac{1}{2}\mathbf{R}|)/a_e] \\ &+ \exp(-2.4|\mathbf{r} - \tfrac{1}{2}\mathbf{R}|/a_e)\}, \end{aligned} \tag{5}$$

where

$$\mathbf{R} = \mathbf{r}_c - \mathbf{r}_b, \quad \mathbf{r} = \mathbf{r}_a - \tfrac{1}{2}\mathbf{R}. \tag{6}$$

Vectors $\mathbf{r}_a$, $\mathbf{r}_b$, and $\mathbf{r}_c$ are positions of the nuclei a, b, and c in the system $\mu a + bc$. Nuclei b and c are components of the homonuclear molecule bc. The Bohr radius of the ''electronic'' hydrogen atom is denoted by a_e. Constant C is of the order of a_e^{-3} [38]. We note that the magnitude of this potential is greater by about 30% than the one obtained for the scattering of muonic hydrogen on hydrogen *atoms* in the framework of the improved adiabatic basis [37]. The formula above contains contributions from the second-order polarization term of the muonic hydrogen-electron interaction. The numerical calculations presented in Ref. [37] take into account only the monopole part of this interaction.

The molecular binding effects are estimated according to the Fermi pseudopotential method, which was used for calculations of the cross sections for slow neutron scattering on protons bound in molecules. A similar method has been developed for the case of muonic hydrogen scattering on hydrogen molecules [38–40]. To calculate the molecular cross sections, the interaction of a muonic hydrogen atom μa with a single hydrogen nucleus b is described by the pseudopotential:

$$V_n(\mathbf{r}_a, \mathbf{r}_b) = \frac{2\pi\lambda_b}{\mathcal{M}_b}\delta(\mathbf{r}_a - \mathbf{r}_b), \tag{7}$$

where $\mathcal{M}_b$ is the reduced mass of the $\mu a + b$ system. The spin-dependent operator λ_b is the elastic or spin-flip scattering length of the *nuclear* process $\mu a + b$. The interaction of the muonic hydrogen atom with the hydrogen molecule is therefore described by the sum of the screening potential (5) and the two potentials (7), corresponding to the presence of the hydrogen nuclei b and c in the molecule bc. The screening potential is relatively weak, so that the electronic contribution to the scattering amplitude practically comes only from distances r of the order of a_e. Since the cross sections for the scattering $\mu a + b$ vary considerably within the energy range of interest, the Fermi model has been improved by replacing the constant scattering length λ_b in the potential (7) by energy-dependent scattering amplitudes [6,41]:

$$\lambda_b \rightarrow \overline{\lambda_b}(p_b) = -f_b(\mathbf{p}_b), \tag{8}$$

where f_b is the amplitude of the scattering $\mu a + b \rightarrow \mu a + b$ and $\mathbf{p}_b$ is μa momentum in the nuclear $\mu a + b$ c.m. system. The values of elements of the reaction matrix T for the scattering $\mu p + p$ and $\mu d + d$, published in Ref. [28], have been used to calculate the elastic and spin-flip scattering amplitudes and therefore to form the respective pseudopotentials.

The molecular cross sections are calculated in the first Born approximation. They are summed over all final rotational and vibrational states of the hydrogen molecule which are possible for a fixed value of the initial μa momentum $\mathbf{P}$, given in the *molecular* $\mu a + bc$ c.m. system. Any fixed momentum $\mathbf{P}$ corresponds to a continuous spectrum of the momentum $\mathbf{p}_b$, due to internal motion of the nucleus b within the molecule. Thus the calculations [41] include averaging over momentum $\mathbf{p}_b$. The eigenfunctions of different initial rotational states and of the ground vibrational state have been used for this purpose. Since one always deals with μa scattering on the zero point vibrations of the target nuclei, a characteristic width of the collisional energy spectrum in the $\mu a + b$ c.m. system (for a fixed P) is of the order of 0.5 eV — the vibrational quantum of H_2. That leads to certain smoothing of the total molecular cross sections, compared to the respective nuclear ones. This effect is important if a scattering amplitude changes rapidly, e.g., near the spin-flip threshold of 0.182 eV in the lower channel of $\mu p + p$ elastic scattering.

The calculated total molecular cross sections differ significantly from the input nuclear cross sections below about 1 eV for collisions preserving the total spin of μa [42]. The

molecular corrections to the total spin-flip reactions are smaller since they are characterized by relatively greater momentum transfers. These differences are more important when one considers the partial differential cross sections. Various rotational transitions in hydrogen molecules involve their specific angular dependencies. The screening potential gives the strongest contributions to the forward scattering. Therefore the molecular differential cross sections are very anisotropic, especially if only a few rotational transitions take place. Some examples of the differential molecular cross sections for the scattering $\mu p+H_2$ and $\mu d+D_2$ have been discussed in Ref. [43].

The present Monte Carlo simulations of the diffusion processes $\mu p+H_2$ and $\mu p+D_2$ have been performed in the laboratory system. The molecular differential cross sections [41,43], calculated in the molecular c.m. system, have been used to derive the laboratory partial differential cross sections (1). These cross sections have been averaged at temperature 300 K over the Boltzmann distribution of the initial rotational levels and over the directions and values of velocities of the target molecules described by the Maxwell distribution. For energies greater than a few eV, the doubled values of the nuclear differential cross sections [28] have been used when calculating the laboratory molecular cross sections.

The accuracy of the molecular cross sections depends on the accuracy of the input nuclear cross sections (see Sec. IVA), the accuracy of determination of the effective screening potential (5), and the errors in the pseudopotential method of estimation of the molecular binding effects. Since the screening potential (5) has been obtained in the second order of the perturbation theory with respect to the parameter $\sqrt{m_e/m_\mu}\approx\frac{1}{14}$, truncation of higher-order terms leads to an error of about 5–10 % of the calculated potential. The influence of this error on the molecular cross sections depends on the muonic atom energy. When the energy approaches zero, the screening interaction is dominant, which leads to the error of about 10–20 % in the molecular cross section. At energies of a few eV the potential (5) can be neglected.

At this time there is no direct estimation of accuracy of the pseudopotential method used for determination of the molecular binding effects in muonic atom scattering on molecules, nor has this problem been solved by another method. The Fermi method can be used in the case of muonic atom scattering since the nuclear scattering lengths (8) are much smaller than the muonic atom wavelengths at low energies and also than the radius of the hydrogen molecule. The pseudopotential method gives good results for neutron scattering on protons bound in chemical compounds, and therefore it is expected that this method also gives reasonable results (error of about 10–20 %) in the case of muonic atoms, though the scattering lengths (8) sometimes depend strongly on collision energy ($\mu p+H_2$, $\mu t+T_2$).

V. SUMMARY AND CONCLUSIONS

The purpose of the experiment was to acquire and interpret the data necessary to understand the history of muonic hydrogen (μp and μd) atoms formed by stopping negative muons in gaseous targets filled with hydrogen or deuterium at pressures between 47 and 1520 mbar. Such pressures are of special interest for experiments in nuclear muon absorption in the upper hyperfine state of the μp or μd atom. Primary goals were the determination of the ''initial'' kinetic energy distributions for the μp or μd atoms when they reached the $1S$ state following the cascade through states lying below those in which the muonic atoms were formed, and the testing of theoretical calculations of the cross sections for scattering of the μp or μd on the molecules of the target gas. The energy distributions which were compared with experiment had to be chosen within the limitations of computational power available for testing the assumed forms for the distributions. At ''low'' pressures about 100 mbar, the initial energy distributions were dominant in producing the observed results. At higher pressures the scattering of the μp or μd dominated the observed data.

With regard to the initial energy distributions, the μd data showed that the two initial energy distributions which are characterized by single parameters, i.e., the δ-function and single Maxwell distributions, both give poor fits to the data. Better fits were obtained from a power energy distribution $E^{-\alpha}$ (with high-energy cutoff), and from the double Maxwell distribution with a thermal component. Furthermore, the mean energy of the nonthermal component of the double Maxwell distribution was sensitive to target gas pressure, rising smoothly from about 1.4 eV at 94 mbar pressure to 3.0 eV at 1520 mbar. This fact, plus the observation that the mean kinetic energy traversed a similar range of values vs pressure for all tested energy distributions, is in support of the idea that a fast component of muonic hydrogen energies is produced collisionally by some acceleration mechanism such as Coulomb deexcitation during the cascade. Finally, the fact that the molecular factor $\mathcal{F}$ is 1.02 for the double Maxwell (and also the power) distribution gives support to the theoretical $\mu d+D_2$ scattering cross sections.

The situation with regard to μp data analysis is not as satisfactory as for μd, in the sense that χ^2 values for the fits are substantially larger than unity in all cases. It is true that still for the μp case the double Maxwell and power initial energy distributions yield χ^2 values which are substantially smaller than for the δ-function or single Maxwell distributions, giving support to the idea that the power and double Maxwell energy distributions are closer to reality. We also note that with all the assumed energy distributions the mean energy rises from about two eV at 47 mbar to 10 eV at 375–750 mbar. (It was noted above that this experiment cannot distinguish among mean energies which are above 10–20 eV.)

Nevertheless, with χ^2 values near 2.0, the power and double Maxwell fits to the μp data are far from satisfactory. Since it is reasonable to suppose that the μp initial energy distribution at a given pressure is similar in form to the distribution for μd, it is puzzling that those distributions (double Maxwell, power) provide poor fits to the μp data, as indicated by χ^2 values of 1.5–2. As indicated above in Sec. IIID, the fit can be improved if the singlet $\mu p+H_2$ cross sections are increased by 20–30 % from the theoretical values over a restricted collision energy range in the neighborhood of 0.1–0.4 eV. The screening contribution for these energies ranges from 130% (at 0.1 eV) to 25% (at 0.4 eV). Since in the case of singlet $\mu p+H_2$ scattering

the signs of the nuclear and electron screening scattering lengths are the same, the presence of electrons leads to an increase of the molecular cross sections. This effect is especially strong at lowest energies because the magnitudes of these scattering lengths are comparable. Thus the cross sections for the process $\mu p + H_2$, calculated in Ref. [37] using a smaller screening potential, would give worse fits than the molecular cross sections used in this paper. However, the fitting results cannot be fully ascribed to the inaccuracy of the screening potential. Another possible explanation is that the pseudopotential method may not work very accurately in the region of the hyperfine cusp in the singlet cross section. Nevertheless, the calculated molecular cross sections lead to the best fits compared to those obtained with nuclear or atomic cross sections, and the binding effects increase the total molecular cross sections by 30% at 0.1 eV and 8% at 0.4 eV.

The influence of the assumed initial μp spin population on the fits has not been investigated. That would have involved introducing more free parameters to the fitting routine. Without experimental evidence to the contrary, our assumption of an initial statistical mixture of hyperfine states in the $1S$ μp atom appears reasonable. We suspect mainly the more complicated structure of the μp cross sections to be the source of the fitting problem.

Finally, we note that the best-fit initial energy distributions for μd and μp atoms indicate that the initial mean energy of the μp is twice that of the μd at pressures near 100 mbar.

With more intense beams now available at PSI, it should be possible to investigate μp effects to even lower pressures. The higher-energy component to the velocity distributions may be studied with foil coating of a low-Z element so that muonic x rays can be used to give superior timing accuracy in the transfer signal. It is to be noted, however, that the results of this experiment already indicate that the μd scattering cross sections and velocity distributions are known well enough for the planning of the experiments on muon capture in deuterium gas.

ACKNOWLEDGMENTS

We wish to acknowledge the support of Dr. H.K. Walter and the staff of PSI (formerly SIN). Also, this work was supported in part by the National Science Foundation under Grants No. PHY-9115407, No. PHY-9300072, No. INT-9119223, and the Polish Committee for Scientific Research under Grant No. 2P03B01809.

[1] L. W. Alvarez *et al.*, Phys. Rev. **105**, 1127 (1957).
[2] G. M. Marshall *et al.*, Hyperfine Inter. **82**, 529 (1993).
[3] A. Alberigi-Quaranta *et al.*, Nuovo Cimento **B47**, 72 (1967).
[4] A. Bertin *et al.*, Nuovo Cimento A **72**, 2118 (1982).
[5] J. B. Kraiman *et al.*, Phys. Rev. Lett. **63**, 1942 (1989).
[6] A. Adamczak *et al.*, At. Data Nucl. Data Tables **62**, 255 (1996).
[7] A. Alberigi-Quaranta *et al.*, Phys. Rev. **47**, B92 (1967).
[8] D. W. Viel, William and Mary Report No. WMHEG 90-1, 1990 (unpublished).
[9] C. T. A. M. de Laat, Rijksuniversiteit Report No. FI 91-1, 1991 (unpublished).
[10] T. Suzuki *et al.*, Phys. Rev. C **35**, 2212 (1987).
[11] V. E. Markushin, Phys. Rev. A **50**, 1137 (1994).
[12] L. I. Menshikov, Muon Catal. Fusion **2**, 173 (1988).
[13] J. E. Crawford *et al.*, Phys. Rev. D **43**, 46 (1991).
[14] E. C. Aschenauer *et al.*, Phys. Rev. A **51**, 1965 (1995).
[15] S. I. Vinitsky and L. I. Ponomarev, Fiz. Elem. Chastits At. Yadra **13**, 1336 (1982) [Sov. J. Part. Nucl. **13**, 447 (1982)].
[16] V. B. Belayev *et al.*, Zh. Éksp. Teor. Fiz. **37**, 1652 (1959) [Sov. Phys. JETP **10**, 1171 (1960)].
[17] S. S. Gerstein, Zh. Éksp. Teor. Fiz. **34**, 463 (1958) [Sov. Phys. JETP **7**, 318 (1958)]; **40**, 698 (1961) [**13**, 488 (1961)].
[18] A .V. Matveenko and L. I. Ponomarev, Zh. Éksp. Teor. Fiz. **59**, 1593 (1970) [Sov. Phys. JETP **32**, 871 (1971)].
[19] A. V. Matveenko, L. I. Ponomarev, and M. P. Faifman, Zh. Éksp. Teor. Fiz. **68**, 437 (1975) [Sov. Phys. JETP **41**, 212 (1975)].
[20] L. I. Ponomarev, L. N. Somov, and M. P. Faifman, Yad. Fiz. **29**, 133 (1979) [Sov. J. Nucl. Phys. **29**, 67 (1980)].
[21] L. I. Ponomarev, in *Proceedings of the VI International Conference on Atomic Physics, Zinante Riga, 1978* (Plenum Press, New York, 1978), pp. 182–206.
[22] M. Bubak and M. P. Faifman, JINR Report No. E4-87-464, 1987 (unpublished).
[23] K. Kobayashi, T. Ishihara, and N. Toshima, Muon Catal. Fusion **2**, 191 (1988).
[24] J.S. Cohen and M. C. Struensee, Phys. Rev. A **43**, 3460 (1991); J .S. Cohen, *ibid.* **43**, 4668 (1991).
[25] M. C. Struensee, J. S. Cohen, and R. T. Pack, Phys. Rev. A **34**, 3605 (1986); **37**, 340 (1988).
[26] V. S. Melezhik, L. I. Ponomarev, and M. P. Faifman, Zh. Éksp. Teor. Fiz. **85**, 434 (1983) [Sov. Phys. JETP **58**, 254 (1983)].
[27] V. S. Melezhik, J. Comput. Phys. **65**, 1 (1986); Muon Catal. Fusion **2**, 117 (1988).
[28] L. Bracci *et al.*, Muon Catal. Fusion **4**, 247 (1989).
[29] C. Chiccoli *et al.*, Muon Catal. Fusion **7**, 87 (1992).
[30] A. A. Kvitsinsky and C. Y. Hu, Phys. Rev. A **47**, 994 (1993); **47**, 3476 (1993).
[31] A. A. Kvitsinsky, C. Y. Hu, and J. S. Cohen, Phys. Rev. A **53**, 255 (1996).
[32] M. Kamimura, Muon Catal. Fusion **3**, 3 (1988).
[33] V. V. Gusev, L. I. Ponomarev, and E. A. Solov'ev, Los Alamos Report No. LA-12698-C, 1993 (unpublished).
[34] A. Adamczak *et al.*, Phys. Lett. A **285**, 319 (1992).
[35] A. V. Kravtsov, A. I. Mikhailov, and N. P. Popov, J. Phys. B **19**, 1323 (1986).
[36] A. Adamczak, V. S. Melezhik, and L. I. Menshikov, Z. Phys. D **4**, 153 (1986).
[37] J. S. Cohen, Muon Catal. Fusion **6**, 3 (1991).
[38] A. Adamczak, Muon Catal. Fusion **4**, 31 (1989).

[39] S. S. Gerstein, Zh. Éksp. Teor. Fiz. **34**, 993 (1958) [Sov. Phys. JETP **7**, 685 (1958)].
[40] L. I. Menshikov, Kurchatov Institute of Atomic Energy, Report No. IAE-3811/12, 1983 (unpublished).
[41] A. Adamczak (unpublished).
[42] A. Adamczak and V. S. Melezhik, Muon Catal. Fusion **4**, 303 (1990).
[43] A. Adamczak, Hyperfine Interact. **82**, 91 (1993).